ENGINEERING

Skin preparation–free, stretchable microneedle adhesive patches for reliable electrophysiological sensing and exoskeleton robot control

Heesoo Kim[1]†, Juhyun Lee[1]†, Ung Heo[2], Dhileep Kumar Jayashankar[3], Karen-Christian Agno[1], Yeji Kim[4], Choong Yeon Kim[1], Youngjun Oh[1], Sang-Hyuk Byun[1], Bohyung Choi[1], Hwayeong Jeong[2], Woon-Hong Yeo[5,6,7,8], Zhuo Li[9], Seongjun Park[4], Jianliang Xiao[3]*, Jung Kim[2]*, Jae-Woong Jeong[1,10]*

High-fidelity and comfortable recording of electrophysiological (EP) signals with on-the-fly setup is essential for health care and human-machine interfaces (HMIs). Microneedle electrodes allow direct access to the epidermis and eliminate time-consuming skin preparation. However, existing microneedle electrodes lack elasticity and reliability required for robust skin interfacing, thereby making long-term, high-quality EP sensing challenging during body movement. Here, we introduce a stretchable microneedle adhesive patch (SNAP) providing excellent skin penetrability and a robust electromechanical skin interface for prolonged and reliable EP monitoring under varying skin conditions. Results demonstrate that the SNAP can substantially reduce skin contact impedance under skin contamination and enhance wearing comfort during motion, outperforming gel and flexible microneedle electrodes. Our wireless SNAP demonstration for exoskeleton robot control shows its potential for highly reliable HMIs, even under time-dynamic skin conditions. We envision that the SNAP will open new opportunities for wearable EP sensing and its real-world applications in HMIs.

INTRODUCTION

The reliable and accurate recording of electrophysiological (EP) signals from the skin is crucial for clinical diagnoses (*1*–*4*), rehabilitation (*5*, *6*), and human-machine interfaces (HMIs) (*7*–*9*). Preparation-free EP sensors with superior recording quality over extended periods regardless of skin conditions are vital and will bring practical impact on a wide variety of real-world wearable applications (*10*–*13*). Conventionally, clinical metal electrodes with conductive gel or electrodes with hydrogel are commonly used for EP sensing owing to their satisfactory signal acquisition performance and cost-effectiveness (*14*, *15*). However, these electrodes require cumbersome preparation steps, such as applying gel and cleaning the skin with alcohol swabs, and they experience signal degradation due to the drying of gel over time (*16*). Furthermore, their interface susceptible to sliding with gel can cause motion artifacts (*17*, *18*). In addition, the conductive gel can potentially induce skin allergies or irritations (*19*–*21*), inhibiting prolonged use of the electrodes.

Advancements in materials and microfabrication techniques have attempted to overcome these limitations by developing soft and dry epidermal electrodes that offer comfortable long-term EP signal monitoring without the need for electrolyte gel (*2*, *3*, *7*, *8*, *11*, *22*–*27*). Nevertheless, without skin preparation such as cleaning and exfoliation, these dry electrodes attached to the skin surface typically exhibit high and unstable skin contact impedance due to factors such as hair, the stratum corneum, and skin secretions (*28*). In addition, epidermal electrodes maintaining contact with the skin solely through van der Waals force can result in an unstable electrode-skin interface during sweating and strenuous movements (*24*, *29*). In some cases of tattoo-like electrodes, device preparation needs additional equipment, such as a stencil mask or spray printer, to print on the skin, hindering the ease of use (*7*, *23*, *30*).

A promising solution to mitigate the vulnerability of EP sensors to skin conditions may be microneedle electrodes. The microneedle electrodes offer a stable electrical interface without needing skin preparation, facilitated by their epidermis accessibility enabled through penetration of microneedles. Previous studies (*11*, *27*, *31*–*36*) have demonstrated flexible microneedle electrodes (FMEs) built on polymer substrates such as polyimide (PI) [2 to 3 GPa (*37*)], polystyrene [2.3 to 3.8 GPa (*38*)], and parylene [1.3 to 3.5 GPa (*39*)]. Although these FMEs are materially biocompatible, their high modulus of the substrate [on the order of gigapascals (*37*–*39*)], which does not mechanically match with skin tissue [60 to 850 kPa (*40*)], leads to interface failure issues and discomfort during long-term wearing. Recent development of stretchable microneedle electrodes using a polydimethylsiloxane [PDMS; 2.6 MPa (*41*)] substrate partially alleviated the modulus mismatch problem. However, these electrodes still encounter challenges in conforming to tissue strain due to their higher modulus than the tissue and lack of adhesion to the

[1]School of Electrical Engineering, Korea Advanced Institute of Science and Technology (KAIST), Daejeon 34141, Republic of Korea. [2]Department of Mechanical Engineering, Korea Advanced Institute of Science and Technology (KAIST), Daejeon 34141, Republic of Korea. [3]Department of Mechanical Engineering, University of Colorado Boulder, Boulder, CO 80309, USA. [4]Department of Bio and Brain Engineering, Korea Advanced Institute of Science and Technology (KAIST), Daejeon 34141, Republic of Korea. [5]IEN Center for Wearable Intelligent Systems and Healthcare at the Institute for Electronics and Nanotechnology, Georgia Institute of Technology, Atlanta, GA 30332, USA. [6]George W. Woodruff School of Mechanical Engineering, Georgia Institute of Technology, Atlanta, GA 30332, USA. [7]Wallace H. Coulter Department of Biomedical Engineering, Georgia Tech and Emory University, Atlanta, GA 30332, USA. [8]Parker H. Petit Institute for Bioengineering and Biosciences, Institute for Materials, Neural Engineering Center, Institute for Robotics and Intelligent Machines, Georgia Institute of Technology, Atlanta, GA 30332, USA. [9]Department of Material Science, Fudan University, Shanghai 200433, China. [10]KAIST Institute for Health Science and Technology, Daejeon 34141, Republic of Korea.
*Corresponding author. Email: jjeong1@kaist.ac.kr (J.-W.J.); jungkim@kaist.ac.kr (J.K.); jianliang.xiao@colorado.edu (J.X.)
†These authors contributed equally to this work.

tissue surface (*42*, *43*). Furthermore, the EP signal recording performance of the previous stretchable microneedle electrode was barely investigated because of difficulties in making electrical connections and insufficient electrical reliability during elongation (*42*, *43*).

Here, we present a stretchable microneedle adhesive patch (SNAP) as a solution for preparation-free, highly reliable, and long-term EP signal monitoring irrespective of skin condition. The stretchable platform with serpentine interconnects of SNAP can accommodate the dynamics of skin tissue and help improve wearing comfort over a long period. Incorporating silicon (Si) microneedle arrays beneath the stretchable interconnects enables their penetration into the stratum corneum, providing direct contact with the epidermis without reaching the pain receptors. This facilitates high-quality EP signal acquisition free from pain and skin preparation. Moreover, the electrically conductive adhesive (ECA) comprising silver (Ag) flakes and high-tack silicone not only enhances the electrode-skin interface by providing an additional conductive path but also ensures secure adhesion to the skin during usage. Through a series of studies, we comprehensively investigated the material, mechanical, and electrical characteristics of SNAPs, confirming their potential for highly reliable long-term EP signal monitoring in various conditions. Finite element analysis (FEA) results and experimental comparisons with other types of EP sensors (e.g., FMEs and gel electrodes) demonstrate that the SNAPs substantially reduce tissue stress during skin deformation and enhance the signal-to-noise ratio (SNR) due to their elastic and penetrable nature. Proof-of-concept demonstrations in the closed-loop operation of an exoskeleton robot highlight the reliability of the skin preparation–free wireless SNAP system, showcasing its potential for HMI applications allowing for quick, seamless setup and freedom of movement for the wearer. We anticipate that the SNAPs will bring a broad impact on applications that require reliable EP sensing, such as continuous health monitoring, neurological research, and wearable HMIs.

RESULTS

Design and working principle of SNAP

Figure 1 illustrates the design concept and operation principle of the SNAP. The SNAP is engineered to have softness, adhesive properties, and tissue adaptability, ensuring long-term and reliable EP signal recording (see table S1 for detailed features and comparison with contemporary microneedle electrodes). The SNAP consists of three primary components (Fig. 1, A and B): (i) stretchable gold (Au) interconnects, (ii) Au-coated Si microneedle array, and (iii) ECA. The stretchable interconnects, designed in a serpentine configuration (5 μm/200 nm/5 μm PI/Au/PI structure), serve as both the electrical and mechanical foundation for the microneedle array. This design renders the overall SNAP elastic, allowing it to dynamically adapt to skin deformation. The rigid Si microneedles [elastic modulus of 130 GPa (*44*)] integrated underneath the serpentine interconnects allow easy insertion through the stratum corneum [10 to 30 μm thick, elastic modulus of 0.525 to 1.05 MPa (*45*, *46*)] to reach the epidermis (*11*, *31*). This architecture ensures low contact impedance, enhancing the performance of the electrode. With the microneedles designed to have a height of 200 μm and a tip diameter of less than 5 μm, pain-free insertion into the skin is ensured as the pain receptors are located below 200 μm from the skin surface (*31*, *47*, *48*). Furthermore, the ECA (45 μm in thickness) surrounding the microneedles provides an additional electrical conductive path from the skin, thereby improving the electrical interface between the electrode and the skin. The ECA consists of high-tack silicone-Ag flakes composite, offering strong adhesion to skin.

Figure 1C highlights the key mechanical feature of the SNAP that enables reliable wearable EP signal monitoring. Because of the soft and stretchable nature of SNAP (effective elastic modulus of 130 kPa, fig. S1), it establishes a robust interface between the microneedles and the skin, accommodating the dynamic skin deformation with minimal mechanical stress to the skin [elastic modulus of 60 to 850 kPa (*40*)]. Experimental and FEA simulation results (Fig. 1, D to F, and movie S1) indicate that the SNAP can stretch over the maximum tensile strain range of human skin [~30% (*8*, *49*)] with negligible relative resistance change (<5%; Fig. 1D) and with only 1.8% maximum principal strain in the metal traces [Fig. 1F, middle; yield strain of Au ≈ 2% (*50*, *51*)]. Note that the majority of the trace area experiences substantially lower strain (<0.5%) compared to the maximum strain. It can also withstand extreme deformations (e.g., 180° twisting with 10% stretching) with high mechanical endurance, experiencing only 0.097% maximal principal strain in the metal traces (Fig. 1, E and F, right). These findings confirm the excellent electrical and mechanical reliability of the SNAP, particularly at strain levels beyond the typical tolerance of human skin (10 to 20%) (*52*). Overall, the unique design integrating the penetrating microneedle array with tissue-conformal elastic electrodes can offer comfortable and highly reliable monitoring of EP signals for long periods of time, minimally interfered from various skin conditions.

Fabrication, material, and mechanical properties of the SNAP

The manufacturing process, depicted in Fig. 2A, highlights the unique fabrication step for integrating rigid microneedle array onto the elastic electrode to create SNAP. Initially, the microneedle array is formed by partial dicing and isotropic wet etching of a Si wafer, followed by titanium (Ti)/Au (20/200 nm) deposition. Afterward, an uncured, low-viscous ECA is poured over the frontside of the Au-coated Si microneedle array. Subsequently, individually isolated microneedles are created by wet etching the bottom side of the Si microneedle array. During the etching process, the ECA layer is protected by the deposited Au layer and the wax applied on the microneedle side. Last, the isolated microneedle array is electrically and mechanically integrated with the serpentine interconnects using conductive epoxy, and the fabrication process concludes by removing the wax. For detailed fabrication steps, refer to fig. S2 and Materials and Methods.

Figure 2B shows the completed SNAP that comprises the stretchable serpentine interconnects (top) and the Au-coated microneedle array with the ECA layer (bottom). The crucial factors for achieving high-fidelity, long-term EP signal recording are excellent epidermis accessibility and a robust electrical and mechanical interface with the skin. The SNAP ensures direct, biocompatible access to the epidermis through the protruding Au-coated microneedle tip, which emerges from the ECA layer (Fig. 2C). Simultaneously, it maintains strong adhesiveness, high stretchability, and low contact impedance through the ECA layer, which is a polymeric composite of surface-modified Ag flakes and high-tack silicone in an optimized ratio [Silbione (5 kPa):Ecoflex GEL (33 kPa) = 1:3; Silbione RT Gel 4717,

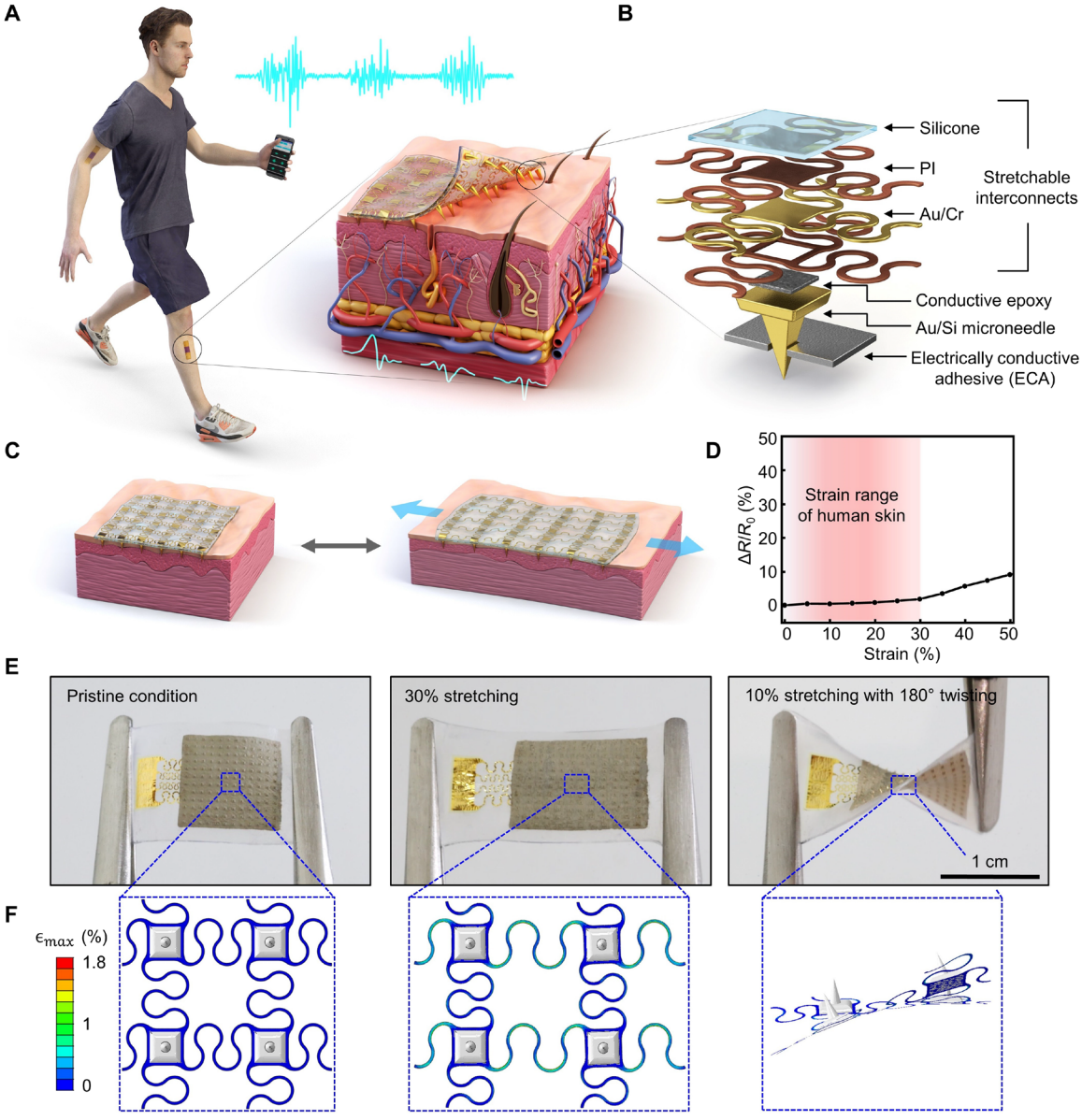

Fig. 1. Design and working concept of the SNAP. (**A**) Schematic illustration showing the overall system configuration and application of SNAP. The patch-type device integrated with skin-conformal SNAP is capable of reliable, long-term EP signal monitoring regardless of skin conditions. The inset shows a close-up view of the soft, tissue-adapting SNAP that uses microneedles to penetrate the stratum corneum for direct access of the epidermis. (**B**) Exploded view schematic diagram of a SNAP, consisting of stretchable serpentine interconnects, Au-coated Si microneedle, and ECA made of Ag flakes–silicone composite. (**C**) Schematic illustration of the SNAP, highlighting its ability to adapt tissue stretching. (**D**) Relative resistance change of the SNAP as a function of tensile strain. The SNAP exhibits negligible resistance change when subjected to 30% stretching, which corresponds to the maximum stretching range of human skin (*8*, *49*). This highlights its ability to maintain stable electrical measurement under tensile deformation. (**E**) Optical images showing high mechanical compliance of SNAP: (left) pristine condition, (middle) 30% stretching, and (right) 10% stretching with 180° twisting. (**F**) Finite element modeling of the SNAP for deformation configurations corresponding to those shown in (E).

Bluestar Silicones; Ecoflex GEL, Smooth-On-Inc. (*53*–*55*)]. Silbione improves the adhesion of ECA, while Ecoflex GEL enhances the toughness. The surface-modified Ag flakes play an important role in enhancing the electrical conductivity of ECA. Through the iodination process, the surface of the Ag flakes is roughened (Fig. 2D), leading to the formation of Ag/AgI nanoislands that expose fresh silver (*54*, *56*). This promotes the sintering among Ag flakes, resulting in an increase in the intrinsic conductivity of the ECA (6580 S/cm, fig. S3). Furthermore, the attained morphology of the two-dimensional surface-modified Ag flakes increases the stretching stability of the ECA through the parallel stacking of adjacent flakes along the substrate plane direction during the curing of the low-viscous conductive polymer (fig. S4A) (*56*). Consequently, the interparticle distance between adjacent flakes is maintained to some extent within a certain strain range (30%), allowing for a reliable electrical conductive path less susceptible to stretching (fig. S4B). This is evidenced

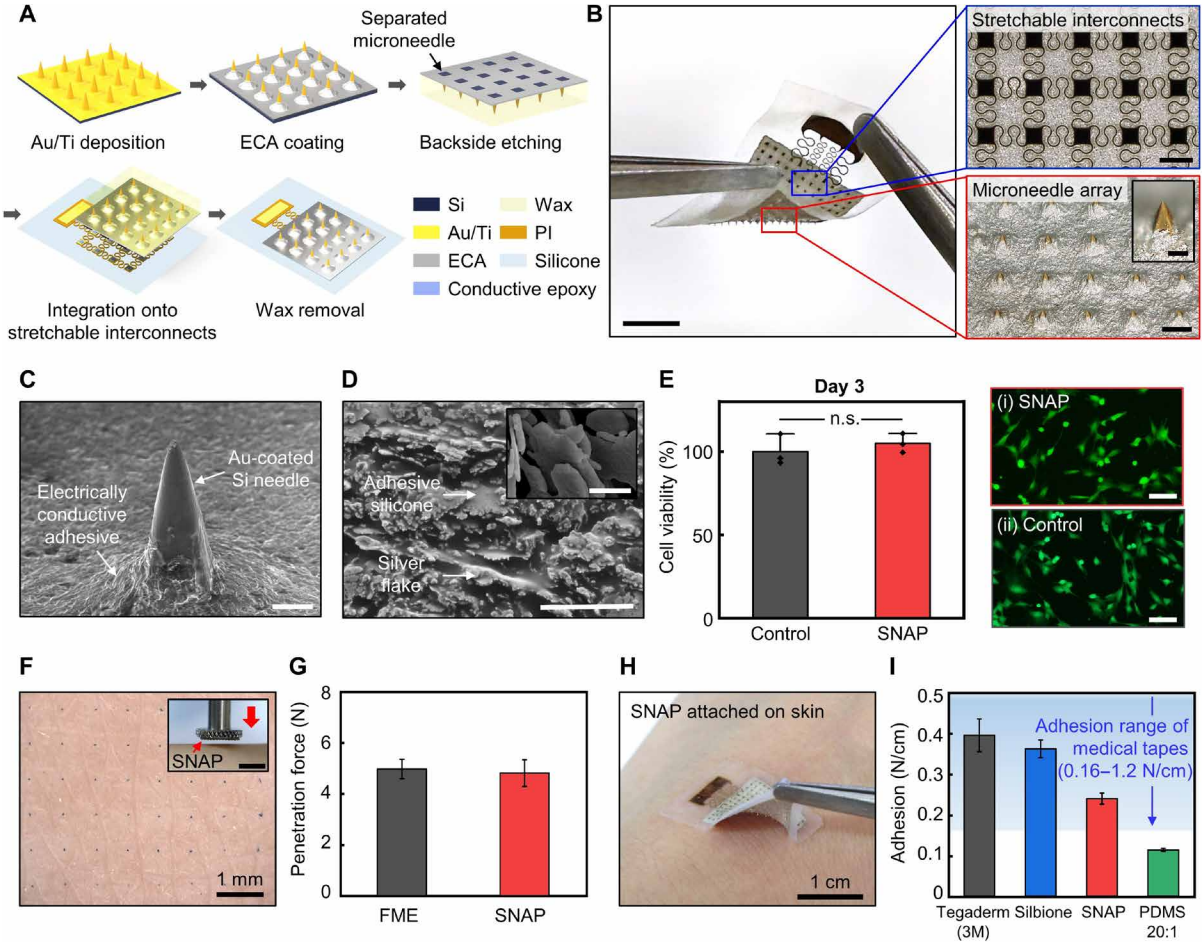

Fig. 2. Fabrication, material, and mechanical properties of the SNAP. (**A**) Schematic illustration of the fabrication process for the SNAP. (**B**) Optical image of the completed device. Scale bar, 5 mm. The images on the right show micrographs of the stretchable interconnects that connect microneedles (top image; backside of the device) and Au-coated microneedle array with ECA substrate (bottom image; frontside of the device). Scale bars, 500 μm. The inset in the red-boxed image shows a magnified view of a single microneedle. Scale bar, 50 μm. (**C**) Scanning electron micrography (SEM) image of a single microneedle showing the Au-coated tip protruding from ECA layer. Scale bar, 50 μm. (**D**) SEM image of the ECA layer showing a mixture of Ag flakes and silicone gel (Silbione:Ecoflex GEL = 1:3). Scale bar, 10 μm. The inset shows the Ag flakes with roughened surfaces. Scale bar, 1 μm. (**E**) Graph comparing the cell viability between the control group (without the SNAP) and the experimental group (with the SNAP immersed) cultured in cell medium on day 3. The images on the right show the live/dead staining images of 3T3 cells after a 3-day culture for the SNAP-immersed group (i) and the control group (ii). Scale bar, 100 μm. (**F**) Optical image of the human skin stained with blue dye coated on the microneedle array. The inset illustrates the experimental setup for skin penetration through the SNAP. Scale bar, 1 cm. (**G**) Graph comparing the skin penetration force for the SNAP in comparison with the FME. (**H**) Optical image of a SNAP mounted on the skin, intentionally partially detached using a tweezer, demonstrating the robust adhesion of the device to the skin. (**I**) Graph showing the adhesion strength of SNAP to the skin compared to the ones of commercial medical film and silicone adhesives (e.g., Silbione, 20:1 PDMS). n.s., not significant.

by a small relative resistance change (~15%) when the ECA is subjected to the allowable maximum tensile strain of human skin (30%, fig. S4C).

The experimental results shown in Fig. 2E explore the on-skin biocompatibility of the SNAP, verifying that our device does not cause any undesirable harm during long-term use. To assess the biocompatibility of the SNAP, a cytotoxicity test was conducted with 3T3 cells (mice embryonic fibroblast cell line). In this test, SNAP was fully immersed in the cell medium and incubated with 3T3 cells. The cells cultured in the SNAP-immersed cell medium exhibited comparable cell viability to the control group with complete cell medium (approximately 100%) on days 3 and 7 (Fig. 2E and fig. S5). Fluorescent live/dead staining clearly demonstrates no notable difference between the control group and the SNAP-immersed group, indicating excellent biocompatibility of our SNAP. Aside from the device biocompatibility, another important aspect to consider is sufficient breathability, ensuring comfortable and skin irritation–free wear while sustaining stable EP signal output (*57*–*60*). On the basis of the permeability test conducted following ASTM E96-95 standards (*60*, *61*), the SNAP exhibits excellent water vapor permeability (8.6 g hour^{-1} m^{-2}, fig. S6), which falls within the range of transepidermal water loss observed in human skin (5 to 10 g hour^{-1} m^{-2}) (*57*, *60*), verifying the on-skin breathability of the SNAP.

One of the key design requirements for the SNAP is to achieve uniform skin penetration with low penetration force despite its soft substrate. Our proof-of-concept demonstration in Fig. 2F illustrates

the capability of the SNAP to penetrate the human skin with an insertion force comparable to that of the conventional FME built on a PI substrate (Fig. 2G). The insertion force obtained for the SNAP (≈4.8 N) is clearly lower than the force required to press an elevator button or attach a postage stamp [≈20 N (*31*)]. In addition, as the loading speed increases, the required insertion force decreases (fig. S7). These results suggest that the SNAP can be easily attached to the skin for robust skin penetration with minimal force, achievable even with a gentle finger pressure alone. Moreover, SNAP provides robust adhesion through the tacky ECA layer after the quick attachment, ensuring a reliable device interface on the skin with sufficient adhesion (0.24 N/cm), which falls within the typical adhesion range of commercial medical adhesive tapes [0.16 to 1.2 N/cm (*62*)] (Fig. 2, H and I). As a whole, the biocompatibility, breathability, and mechanical characteristics of the SNAP indicate that it can offer users a comfortable and skin-friendly interface while maintaining an excellent intimate device-skin contact.

Electrical characteristics of the skin-mounted SNAP

Figure 3A illustrates a comparison of the circuit models for the electrode-skin interface of SNAP (iv) with those of other electrode types, namely, gel electrode (i), ECA electrode (ii), and FME (iii). Note that FME was produced by sputtering Ti/Au (20/200 nm in thickness) on a PI-based microneedle electrode, but it does not incorporate an ECA layer, different from SNAP. Various parameters in the circuit models are defined in note S1. Unlike surface electrodes, microneedle electrodes (such as FME and SNAP) circumvent the effects of the double-layer capacitance (C_d) and charge transfer resistance (R_d) at the electrode-tissue interface (*63*). This is achieved by directly accessing the epidermis layer through the penetration of the highly resistive stratum corneum ($>10^5$ ohms) (*39*). In the case of the SNAP, the ECA layer surrounding the microneedle array further enhances the electrode-tissue interface by reducing the contact impedance. Specifically, the contact impedance is reduced by 25% at 100 Hz compared to the FME (Fig. 3B). This reduction aligns with the theoretical analysis derived from the electrode-skin interface equivalent model, as described in note S1. In addition, regardless of skin condition, the SNAP exhibits lower and consistent skin contact impedance (21 ± 5 kilohm·cm^2 at 100 Hz, mean ± SD) in comparison to other electrode types (Fig. 3, B and C, and fig. S8). In multiple sample trials ($n = 5$), the direct epidermis access provided by SNAP results in a stable and notably lower SD (σ) of skin contact impedance (σ_{SNAP} and $\sigma_{FME} \approx 5$ kilohm·cm^2), compared to that of conventional gel or ECA electrodes (σ_{gel} and $\sigma_{ECA} \approx 150$ kilohm·cm^2), irrespective of skin conditions (Fig. 3D). This feature indicates that SNAP can eliminate the need for skin preparation, such as cleaning and exfoliating, as it consistently delivers reliable electrical performance.

Figure 3E provides a visual comparison of the mechanical adaptability between the skin-mounted SNAP and FME when the skin is compressed or stretched. The elastic nature of the SNAP allows it to respond and accommodate dynamic deformations, enabling consistent and stable contact with the skin. In contrast, the FME tends to delaminate from the skin due to the mechanical mismatch at the device-skin interface. FEA results in Fig. 3F show considerably less local stress in the surrounding tissues of the SNAP (0.22 MPa) compared to the FME (0.57 MPa), further verifying that the SNAP can conform to tissue deformation and minimize tissue damage during dynamic motion. Moreover, our experimental measurements of skin contact impedance under strain (Fig. 3G) indicate that the adapting and intimate tissue interfacing of the SNAP reduces the likelihood of creating physical gaps between the electrode and the skin, facilitating the maintenance of a stable skin contact impedance with minimal increases (increase of the contact impedance <5 kilohm·cm^2 at the applied strain of 30%).

To ensure the electrical performance and mechanical compliance of SNAP for long-term use, we monitored the electromyogram (EMG) baseline noise while the device was attached to the skin under repeated cyclic deformation (*64*). Figure 3H shows that the SNAP maintains a consistent EMG baseline noise even after 100 cycles of repeated stretching and compressing (with 30% strain) at the attachment site, confirming robust interface of the SNAP with the skin during dynamic motion. The tissue-adapting interface of the SNAP gives negligible stress to the skin, resulting in unnoticeable red rashes, in contrast to the FME that exhibits visible skin redness after 150 cycles of 30% stretching and releasing (Fig. 3I). To assess the long-term wearability of the SNAP, we attached the SNAP to the flexor carpi radialis muscle in the forearm and monitored changes in the EMG baseline noise over 8 days. We compared these results to those obtained using the ECA electrodes and the commercial gel electrodes (TYH-WF25RP, Skyforever). During the 8-day measurement period, the output signal of the SNAP and the ECA electrode remained stable, with minimal change in baseline noise value (<10%). In contrast, the commercial gel electrode showed a notable increase in baseline noise (69% increase from day 1 to 8) due to electrode drying (Fig. 3J and fig. S9). While it is recommended to clean the skin using water or an alcohol swab to reduce the risk of infection during the initial attachment of SNAPs, these findings collectively demonstrate that the SNAP has unique capabilities enabling robust, long-term monitoring of EP signals regardless of skin conditions and deformation.

Wireless SNAP system for reliable EMG monitoring during dynamic motions

By integrating SNAPs with a stretchable wireless EP signal processing circuit, we have established a wireless SNAP system that enables reliable EMG sensing during dynamic motions (Fig. 4A). The highly conformal nature of the SNAP system to targeted curvilinear muscle areas, such as upper and lower limbs, allows for reliable EP signal recording. Moreover, the wireless feature of the device eliminates the need for conventional bulky and wired setups. The detailed design is as follows:

The serpentine structure [50 μm/36 μm/50 μm PI/Copper (Cu)/PI structure] of the circuit interconnects enables stretchability of the device, with integrated components including a Bluetooth low-energy System-on-Chip (BLE SoC; EYSHSNZWZ, Taiyo Yuden) and an amplifier chip (gain = 200, band-pass filter with passband cutoff frequencies of $f_L = 10$ Hz and $f_H = 1$ kHz; RHA2116, Intan technologies) (fig. S10). The BLE SoC facilitates wireless communication with a portable electronic gadget (e.g., smartphone), allowing for real-time multichannel EP signal monitoring through a user-friendly interface application (maximum number of simultaneous measurement channels = 4) (fig. S11). To ensure optimal comfort and usability, the SNAP system is encapsulated in a silicone elastomer encapsulation (750 μm thick; 69 kPa; Ecoflex 00-30, Smooth-On-Inc.), providing a skin-like softness and high compliance to the tissue movement, particularly during bending and stretching of the target muscle region (figs. S10 and S12). Powering

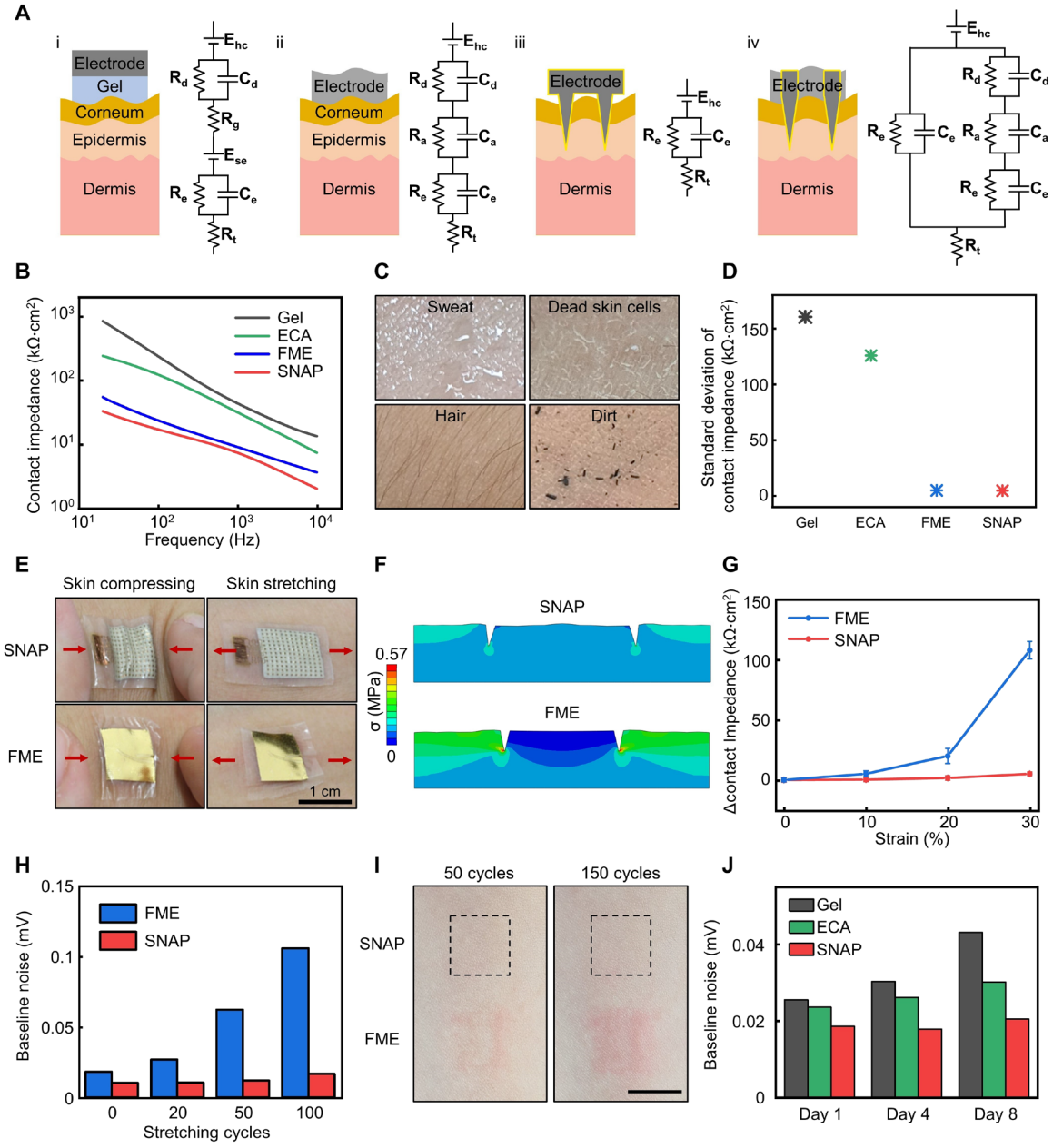

Fig. 3. Electrical characteristics of the SNAP attached to skin. (**A**) Schematic diagram illustrating electrode-skin interfaces for different types of electrodes, along with corresponding equivalent circuit models: (i) gel electrode, (ii) ECA electrode, (iii) FME, and (iv) SNAP. Parameters in the circuit models are defined in note S1. (**B**) Plot of electrode-skin contact impedance changes as a function of frequency. The skin was prepared by wiping it with water-soaked gauze for cleaning, followed by another wipe with an alcohol swap for disinfection. (**C** and **D**) Optical images showing different skin conditions, including the skin with sweat, dead skin cells, hair, and dirts (C), and plot of the SD of skin contact impedance measured with different EP sensors in these various skin conditions (D). (**E**) Photographs of the skin-mounted SNAP and FME captured during skin compression and stretching. (**F**) FEA results visualizing the mechanical stress induced in skin tissue by microneedles of SNAP and FME under uniaxial skin strain ($\varepsilon = 30\%$). (**G**) Plot showing measurements of skin contact impedance of SNAP and FME at varying tensile strains. (**H**) Plot comparing the baseline noise levels of the resting EMG signals measured using SNAP and FME during cyclic stretching and releasing. (**I**) Optical images of the skin surface after cyclic stretching and releasing with SNAP and FME (left, after 50 cycles; right, after 150 cycles), visually indicating that the SNAP imposes negligible stress to the skin due to its high mechanical adaptability. Scale bar, 1 cm. (**J**) Plot comparing the baseline noise levels of the resting EMG signals measured using the SNAP, ECA, and commercial gel electrodes over a period of 8 days.

the device is a modular rechargeable lithium polymer (LiPo) battery, which connects to the stretchable electronic circuit of the SNAP system via a metal pin connector. In addition, the metal opening at the bottom side of the stretchable circuit of the SNAP system provides an electrical connection to the SNAP via an anisotropic conductive film cable and a magnetic connector (fig. S13), allowing for the semipermanent use of the circuit and easy replacement of the SNAPs.

Figure 4B shows the images of the completed wireless SNAP system, demonstrating the device's remarkable mechanical compliance

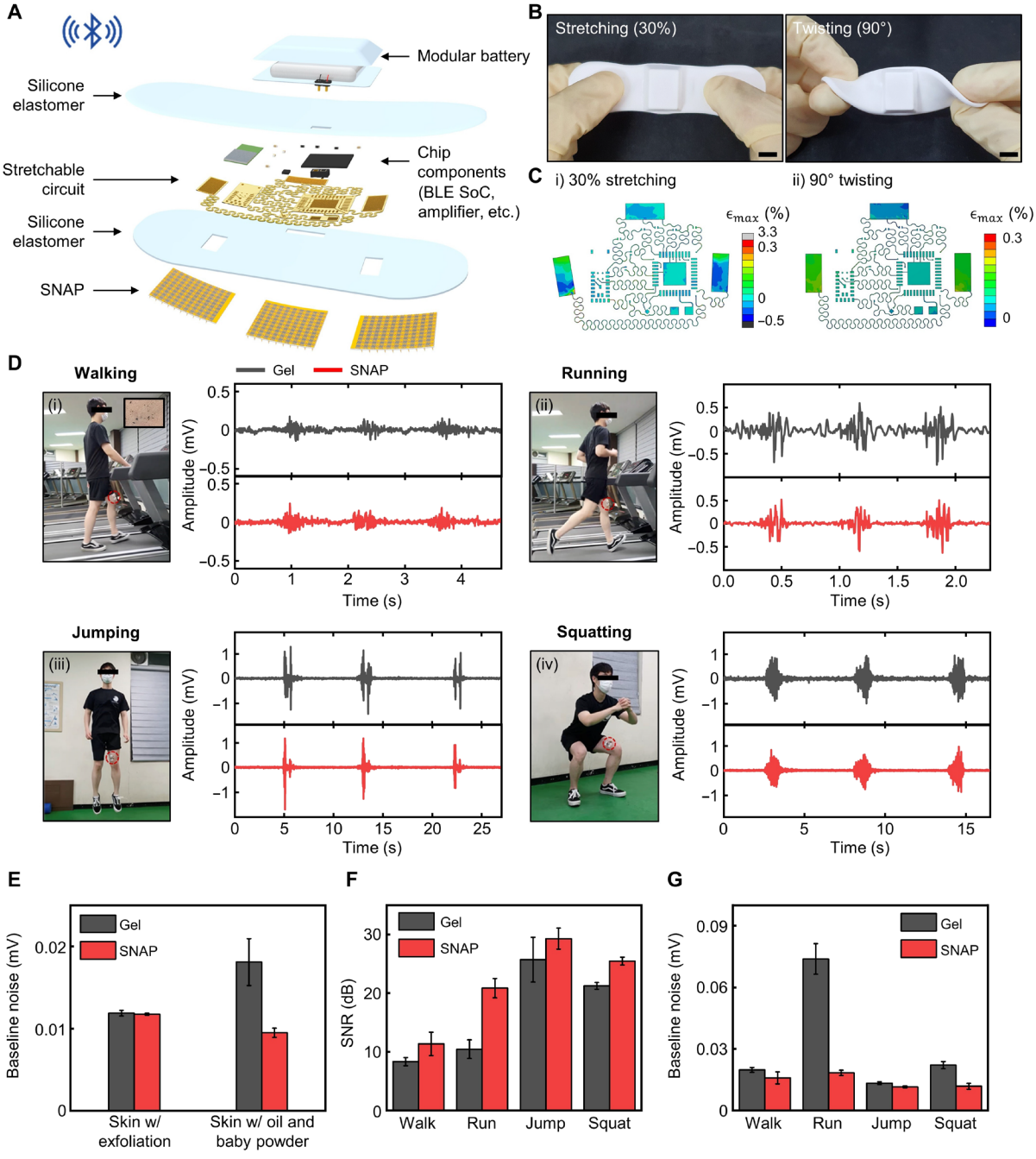

Fig. 4. EMG monitoring performance of the wireless SNAP system during various ambulatory motions. (**A**) Exploded view schematic diagram of the wireless SNAP system. The wireless system consists of SNAPs, a stretchable circuit for wireless EP recording, a detachable LiPo battery encapsulated with soft, biocompatible elastomer. (**B**) Photographs of the device captured during stretching ($\varepsilon = 30\%$; i) and twisting (torsion of 90°; ii). (**C**) FEA simulation results for the device under deformation corresponding to (B). (**D**) Images showing different types of ambulatory motion and their corresponding EMG recording using the patch-type device integrated with gel electrodes (gray plot) and SNAPs (red plot). The human subject performed four types of ambulatory motions: (i) walking, (ii) running, (iii) jumping, and (iv) squatting, with the target muscle being Vastus medialis. (**E** to **G**) Plots of the recorded EMG signal quality, including the baseline noise amplitudes of both pretreated and contaminated skin conditions (E), SNR values (F), and baseline noise amplitudes in four types of ambulatory motion (G).

during dynamic deformations (left image, 30% stretching; right image, 90° twisting). FEA simulations, presented in Fig. 4C, demonstrate that the maximum principal strain of Cu interconnect trace (3.3%) remains below the fracture threshold [fracture strain of Cu ≈ 5% (*65*)] across all regions under deformations. Note that most regions undergo substantially less strain (<0.3%) compared to the maximum strain. This confirms the device's ability to maintain its structural integrity during operation.

To evaluate the potential utility of the wireless SNAP system for EP recording during intense physical activities, which often lead to

dynamic tissue deformation and skin secretion, we monitored the EMG signals while attaching the device to the muscle of a human subject's leg (target muscle: Vastus medialis) during exercise. To simulate the skin secretion during exercise in harsh external conditions, we applied oil and baby powder on the attachment site for EP signal monitoring. Then, we compared the measurement results obtained with the wireless SNAP system to those obtained with a wireless device integrated with conventional gel electrodes. Figure 4D provides examples of various ambulatory exercises, including walking, running, jumping, and squatting, along with their respective EMG measurements. For light physical activity such as walking, the influence of motion artifacts is not notable, and no considerable differences are observed in the EMG signals measured with the SNAPs and gel electrodes (Fig. 4D, i). However, during vigorous exercise such as running and jumping (Fig. 4D, ii and iii), the leg's movement exposes the attached wireless devices (integrated with SNAPs and gel electrodes) to substantial accelerations, tremors, and tissue deformation. The measurements in Fig. 4D (ii and iii) indicate that the SNAP system during running or jumping causes minimal baseline wandering and motion artifacts, while the gel electrode system results in noticeable fluctuations in EMG signals. Besides, under conditions of intentional skin contamination using oil and baby powder, the SNAP shows more robust performance, substantially reducing the baseline noise (47% lower than gel electrodes, 73% lower than ECA electrodes) compared to the other electrodes, demonstrating that our device can withstand skin contamination (Fig. 4, D and E; fig. S14; and movie S2). This trend unaffected by skin conditions was observed not only in EMG but also consistently in other EP signals, such as electroencephalogram, which has much lower signal amplitudes than EMG signals (fig. S15). The robustness of the SNAP system for EMG signal monitoring during ambulatory exercise is further demonstrated by its improved SNR and suppressed baseline amplitude during these dynamic motions compared to the gel electrode, as depicted in Fig. 4 (F and G). Furthermore, the SNAP with ECA showed negligible sensitivity to vibrations, in comparison to the gel electrode and FME, demonstrating its excellent immunity to motion artifacts (fig. S16). The overall results presented here provide strong evidence of the wireless SNAP system's ability to offer high-fidelity EP signal measurements under dynamic motions, suggesting its potential for diverse applications in health care, athlete training, musculoskeletal rehabilitation, and HMI.

Application demonstration of closed-loop EMG control for an exoskeleton robot using the wireless SNAP system

EMG-based exoskeleton robot technology offers the advantage of rapidly recognizing user movement attempts, surpassing conventional kinetic-based exoskeleton robotics by 30 to 100 ms (*66*). It also allows for user input and feedback integration through neuromuscular links (*67*). However, signal instability caused by subject movement and skin secretion poses challenges to the practical use of EMG-based assistive robot control (*67*). In addition, the cumbersome wired sensor system necessitates extensive setup time and restricts the user's natural movement range, confining the exoskeleton robot's application to laboratory settings (*68*).

To overcome these issues, this study presents an exoskeleton robot control empowered by the preparation-free, low-profile, and wireless SNAP system developed for intelligent neuroprosthetics, manual labor assistance, and other HMI fields. We demonstrate the wireless EMG-triggered closed-loop control of a back-supporting exoskeleton robot designed for lifting external loads using the SNAP system. Figure 5 (A and B) provides an overview of the robotic assistance strategy and the system configuration using the wireless SNAP system. The EMG signals are monitored using attached SNAP systems on the lower limb muscles [target muscle: Gluteus maximus (GM) for squat lifting, Biceps femoris (BF) for stoop lifting], triggering the operation of the assistive robot when the signals exceed a preset threshold (Fig. 5C). The SNAP system's excellent immunity to skin perspiration and deformation, compared to conventional gel electrodes, provides a robust sensing interface during dynamic HMI operations (fig. S17). The collected EMG signals are transmitted to a finite state machine in a microcontroller unit and rectified by Teager-Kaiser Energy Operator (TKEO) (*69*), determining the current state of the exoskeleton robot to establish whether it is in assistive mode. This process generates a corresponding torque profile. The assistive torque is conveyed to the hip joint of the user through the closed-loop pneumatic controller, using the desired pneumatic pressure obtained from the actuator inverse model. This assistive strategy prevents musculoskeletal disorders by reducing muscle overexertion and fatigue resulting from repetitive lifting of heavy loads (*68*, *69*). Furthermore, an additional wireless SNAP system is attached to the back muscle, where the target muscle is located [L1 vertebral level of Longissimus thoracis (L1)]. This SNAP system communicates with a smartphone to evaluate the performance of the exoskeleton robot by analyzing the reduction in root mean square of EMG (RMS EMG). The detailed hardware configurations and control architectures are shown in Fig. 5B and fig. S18.

Figure 5C and movie S3 present a proof-of-concept demonstration of the assistive capabilities of the exoskeleton robot integrated with wireless SNAP systems for closed-loop control, showing lifting of a 10-kg load. The experiments encompassed scenarios involving both pretreated skin (with hair removal and alcohol swab wiping) and non-pretreated, perspiring skin conditions, aiming to evaluate the performance of the SNAP system in scenarios that require no prior preparation. The RMS EMG measurements taken from the L1 muscle during exoskeleton operation via the SNAP systems reveal a notable decrease of muscle activation (18.1% in both pretreated skin and non-pretreated, perspiring skin conditions on average), when compared to the cases without robotic assistance. This reduction is consistent across conditions with and without skin preparation and perspiration (Fig. 5D). These results indicate that the SNAP system effectively addresses challenges related to unstable EMG recordings due to subject movement and skin secretions, which have traditionally impeded EMG-based exoskeleton robot control. Furthermore, the exoskeletal robot equipped with the SNAP system exhibits a positive impact on muscle fatigue, underscoring its potential to improve functional mobility for individuals requiring assistance in lifting heavy objects. Comprehensively, the integration of a preparation-free, wireless EP signal monitoring system into an assistive exoskeleton robot presents a promising solution for HMIs, particularly in the domain of wireless prosthetic controls, contributing to physical human augmentation.

DISCUSSION

This work explores the concept and design strategies of SNAP for skin preparation–free and long-term EP signal monitoring. EP sensors with rigid microneedles offer effortless skin penetration but

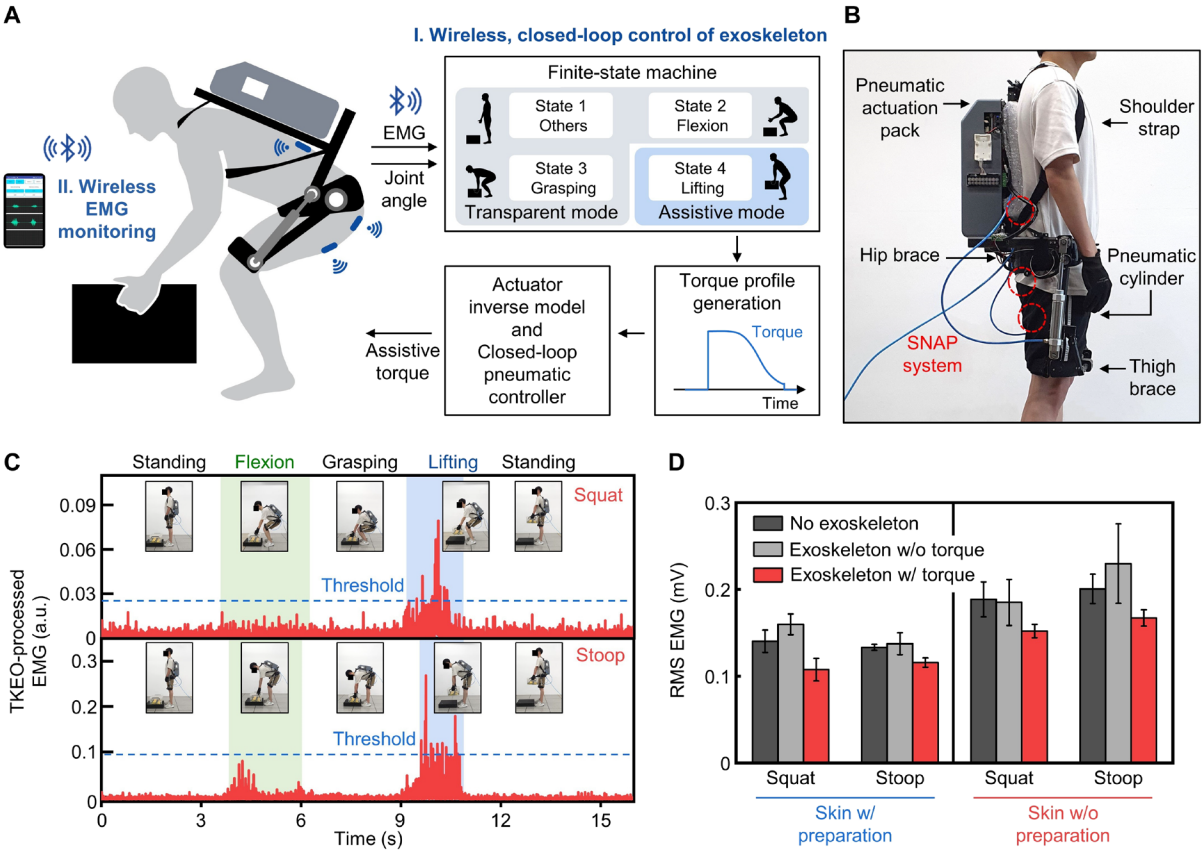

Fig. 5. Demonstration of the wireless SNAP system as an HMI for closed-loop control of an exoskeleton robot. (**A**) Illustration depicting the system architecture and control strategy of an exoskeleton robot. SNAP systems attached to lower limb muscles wirelessly transmit EMG signals to the exoskeleton robot controller to trigger the assistance operation. Another SNAP system attached to the back muscle monitors the muscle activity to evaluate robotic assistance performance. (**B**) The hardware configuration of the pneumatic back support exoskeleton system. Linear actuation of a pneumatic cylinder caused the device to push the trunk, generating an assistive hip joint torque for lifting heavy external loads. SNAP systems attached to the L1, GM, and BF muscles to operate the exoskeleton robot and validate its assistive performance. (**C**) Real-time measurement of TKEO-EMG signals from the trigger muscle during a single cycle of squat lifting (top) and stoop lifting (bottom). (**D**) Comparison of RMS EMG with and without robotic assistance. The back muscle activity was substantially reduced when using robotic assistance, regardless of skin preparation and perspiration levels (average reduction of 18.1% in both pretreated skin and non-pretreated and perspiring skin conditions). a.u., arbitrary units.

may lead to side effects such as skin irritation and rash due to mechanical mismatch, while sensors with soft microneedles accommodate tissue dynamics but can hinder robust, uniform skin penetration, posing challenges for obtaining high-quality EP signals. The rigid-soft hybrid structure of the SNAP, comprising penetrable rigid microneedle arrays and a soft, stretchable adhesive platform, demonstrates unique features, such as direct epidermis accessibility through the stratum corneum and tissue conformability. These attributes not only ensure high immunity to skin secretion and contamination but also offer comfortable wearability over extended periods of time. The SNAP with ECA provides an improved robust on-skin interface due to its high conductivity and adhesiveness, highlighting its reduced motion artifact and baseline noise compared to commercial gel electrodes. Demonstration of the wireless closed-loop operation of an exoskeleton robot with the SNAP system further validates practical utility of the device in sophisticated, real-world HMI applications. For wide deployment, new materials and simpler fabrication methods suitable for mass production will need to be investigated to reduce the cost and complexity associated with the current fabrication approach, which relies on the microelectromechanical systems (MEMS) process. Furthermore, the development of stretchable electrodes with stiffness-tunable microneedles, which are rigid for easy skin penetration and become soft afterward for tissue adaptation, would be essential for completely eliminating the mechanical mismatch at the microneedle-skin interface, ensuring imperceptibly comfortable long-term wear.

MATERIALS AND METHODS

Fabrication of SNAP

Figure S2 illustrates the step-by-step fabrication process for the SNAP. A 4-inch, low-resistivity Si wafer (p-type, 400 μm thick, <0.005 ohm·cm) was used as a base substrate. The fabrication began with forming a hard mask (Si_3N_4, 500 nm) on the Si wafer using plasma-enhanced chemical vapor deposition. The microneedle array was created in a two-step dicing and isotropic etching. First, the Si wafer was partially diced into a square pillar (90 μm width, 300 μm height) array with a pitch of 710 μm using a custom dicing saw (500 μm width, DHK). Then, the array was further diced to form a podium shape, with the pillar on a cuboid base (300 μm width and

depth, 50 μm height). Last, the diced wafer with Si_3N_4 mask on top was immersed in isotropic wet etchant ($HF:HNO_3:CH_3COOH$ = 3:25:10 in volume ratio) for 15 min. This step results in an array of microneedles with a height of 200 μm. To improve the electrical conductivity of the device, a layer of Ti/Au (20 nm/200 nm thick) was sputtered on the front side of the microneedle array.

The ECA was prepared by mixing surface-modified Ag flakes (particle size: 10 μm, Sigma-Aldrich), silicone elastomer (Ecoflex GEL:Silbione = 3:1 in weight ratio), and hexadecane (Sigma-Aldrich) in a 3:1:2 weight ratio for 3 hours. The resulting conductive polymer was spin-coated onto the microneedle arrays (200 rpm), followed by curing at 165°C for 90 min. There was negligible ECA residue left on the microneedles, as ECA aggregated into the microneedle base during solvent evaporation. The microneedle array with a layer of ECA was attached to a Teflon sheet with mounting wax (BJ7, Sharon Chemical) to protect the microneedle arrays from the acid agents. The remaining Si and Au layers on the backside of the microneedle array were chemically removed ($HF:HNO_3$ = 1:4 for Si etch; standard Au etchant for Au etch). Last, the microneedle arrays were rinsed with deionized (DI) water for 12 hours.

The stretchable serpentine interconnects were used to establish the electrical connection between the ECA-coated microneedle array and the wireless circuit module. The interconnects were fabricated using the e-beam evaporation and standard photolithography and then were transferred onto a silicone elastomer (Ecoflex, Smooth-on Inc.) (*8*). The serpentine interconnects were attached to the backside of the microneedle array by screen-printing a layer of conductive epoxy (MED-H20E, Epoxy Technology) using a metal stencil mask (300 μm–by–300 μm square openings with an 800-μm pitch in between) to achieve both electrical and mechanical connections. When the conductive epoxy is properly applied, it establishes electrical connections to both the back of the Si microneedle bases and the gold deposited on the sidewall of the microneedle bases (fig. S2B). The transparent nature of interconnects facilitates easy alignment under a microscope in the attachment process. Last, the wax that covered the microneedle array was removed by thermal heating (120°C, 5 min), followed by a 6-hour rinsing in DI water.

In vitro biocompatibility studies

The in vitro cell viability test was performed using 3T3 cells (mice embryonic fibroblast cell line). The complete medium was made with 10% fetal bovine serum and 1% of penicillin-streptomycin in Dulbecco's modified Eagle's medium. The 3T3 cells were plated on 48-well plates at a density of 2×10^3 cells with a complete medium. The SNAP was entirely immersed into the complete medium and incubated for 7 days with the seeded cells. The seeded cells were stained with a live/dead viability/cytotoxicity kit for mammalian cells (Thermo Fisher Scientific, L3224). The cell viability results were then quantified using excitation/emission wavelengths at 485/530 nm for live cells and 530/645 nm for dead cells by a microplate reader (SpectraMax iD3, Molecular Devices).

Penetration force measurement

A biocompatible blue dye (LIQUA-GEL, Chefmaster) was coated on the microneedle electrode before the measurement to visually verify the penetration of the device into the skin. The backside of the microneedle electrode was secured onto the load cell of the force gauge (ESM303, Mark-10), with the tips facing downward and the subject's forearm was positioned beneath. The load cell was lowered at a constant speed of 15 mm/min with an increasing applied force through each sample. After each trial, the microneedle electrode was removed, and the skin was rinsed. The penetration force of the microneedle electrode to penetrate the stratum corneum was determined as the minimum force applied during the trials where dye marks remained visible for all microneedles in the washed skin and measured by the force gauge (ESM303, Mark-10).

Adhesion force measurement

The adhesion strength between the device and the skin was measured by the standard 90° peeling test using a force gauge (ESM303, Mark-10). The sample devices (2 cm width) were attached to the hairy forearm skin of the human subjects without any skin preparation. A PI film was attached on top of the samples to avoid the stretching of the sample device during peeling. The adhesion strength of the device attached to the skin was determined by dividing the average force (in newtons) by the width (in centimeters) of the bonded pad.

Mechanical modeling and FEA

The stress and strain data for the SNAP and the stretchable circuit in Figs. 1, 3, and 4 were obtained through simulations conducted using the commercial FEA software (Abaqus, Dassault Systèmes). The PI and metal layers were modeled using four-node shell elements (S4R), while the other materials were simulated using eight-node, 3D hexahedron elements (C3D8R).

Skin contact impedance measurement

The electrode-skin contact impedance was obtained using an LCR meter (E4980AL, Keysight Technologies) with a frequency range from 20 Hz to 1 kHz. All the electrodes have the same size of 1 cm by 1 cm. Each pair of electrodes was placed on the forearm of the subject, with a 5-cm spacing between the electrode pair. All measurements were conducted under the same conditions stated earlier.

Design and fabrication of wireless EP monitoring circuit

The wireless circuit patch processes EP signals obtained from electrodes and transmits the signals wirelessly to a smartphone. It consists of a multichannel amplifier with programmable bandwidth (RHA2116, Intan technologies), a low-dropout regulator (NCP161AMX300TBG, Onsemi), and a BLE SoC (EYSHSNZWZ, Taiyo Yuden). All electrical components were mounted on the flexible printed circuit board (PCB) using a low-temperature solder paste (SMDLTLFP10T5, Chip Quik), and they were soldered in a reflow oven (AS-5060, SMTmax). The stretchability of the circuit was achieved by the serpentine-shaped traces (PI/Cu/PI, 50 μm/36 μm/50 μm) fabricated by laser cutting. The wireless circuit was powered by a modular LiPo battery (GM351317, 38 mAh, PowerStream Holdings Inc.), which can be assembled through the male/female pin connectors (M50-3630342/M50-3630242, Harwin Inc.). Last, the fabrication of the wireless patch was completed by encapsulating the circuit with 750-μm-thick soft silicone (Ecoflex 00-30, Smooth-on Inc.; Silbione RT Gel 4717, Bluestar Silicones) using a 3D-printed mold (B9 Core Med 550, B9Creations).

EMG-based closed-loop control of an exoskeleton robot

Two wireless SNAP systems were placed on the right hip (target muscle: GM) and on the right hamstring (target muscle: BF) of a

human subject to trigger the mechanical assistance for two scenarios: squat lifting and stoop lifting. When the TKEO-processed EMG amplitude of the target muscle exceeds the threshold value as the wearer attempts to move (e.g., squat-lift or stoop-lift), the assistance of the exoskeleton robot is triggered (*69*). The SNAP system wirelessly transmitted measured EMG signals to the central microcontroller unit (myRIO-1900, National Instruments Corp.), where the TKEO process was carried out. The finite state machine architecture in the central microcontroller unit determined the current state of the assistive exoskeleton robot, and a desired hip joint torque profile was then generated. The actuator inverse model provided the target pneumatic pressure information through the desired torque profile, which the closed-loop pneumatic controller then used to deliver the appropriate assistive torque to the user's hip joint. Another SNAP system was placed on the back (target muscle: L1), which is used to evaluate the assistive performance of the exoskeleton robot by monitoring the muscle activity. This SNAP system transmitted the measured EMG signal to the smartphone and was used to compare the degree of muscle activity in three cases: (i) no wear of the exoskeleton robot, (ii) wear of the exoskeleton robot without assistive torque, and (iii) wear of the exoskeleton robot with assistive torque.

Experiments on human subjects

All experiments on human subjects were performed under approval from the Institutional Review Board at Korea Advanced Institute of Science and Technology (protocol number: KH2021-070) and received informed consent from the volunteer subjects.

Statistical and data analysis

Statistical analysis in Fig. 2E was conducted with OriginPro. The normality of sample distributions was verified with a Shapiro-Wilk normality test. The homogeneity of covariance was tested with an F test. If these tests were passed, statistical significance was measured with two-sample *t* tests.

Supplementary Materials

This PDF file includes:

Note S1
Figs. S1 to S18
Table S1
Legends for movies S1 to S3
References

Other Supplementary Material for this manuscript includes the following:

Movies S1 to S3

REFERENCES AND NOTES

1. H. Joo, Y. Lee, J. Kim, J.-S. Yoo, S. Yoo, S. Kim, A. K. Arya, S. Kim, S. H. Choi, N. Lu, H. S. Lee, S. Kim, S.-T. Lee, D.-H. Kim, Soft implantable drug delivery device integrated wirelessly with wearable devices to treat fatal seizures. *Sci. Adv.* **7**, eabd4639 (2021).
2. J.-W. Jeong, M. K. Kim, H. Cheng, W.-H. Yeo, X. Huang, Y. Liu, Y. Zhang, Y. Huang, J. A. Rogers, Capacitive epidermal electronics for electrically safe long-term electrophysiological measurements. *Adv. Healthc. Mater.* **3**, 642–648 (2014).
3. N. Rodeheaver, R. Herbert, Y. Kim, M. Mahmood, H. Kim, J. Jeong, W. Yeo, Strain-isolating materials and interfacial physics for soft wearable bioelectronics and wireless, motion artifact-controlled health monitoring. *Adv. Funct. Mater.* **31**, 2104070 (2021).
4. S. Kwon, H. S. Kim, K. Kwon, H. Kim, Y. S. Kim, S. H. Lee, Y.-T. Kwon, J.-W. Jeong, L. M. Trotti, A. Duarte, W.-H. Yeo, At-home wireless sleep monitoring patches for the clinical assessment of sleep quality and sleep apnea. *Sci. Adv.* **9**, eadg9671 (2023).
5. K. Bayoumy, M. Gaber, A. Elshafeey, O. Mhaimeed, E. H. Dineen, F. A. Marvel, S. S. Martin, E. D. Muse, M. P. Turakhia, K. G. Tarakji, M. B. Elshazly, Smart wearable devices in cardiovascular care: Where we are and how to move forward. *Nat. Rev. Cardiol.* **18**, 581–599 (2021).
6. G. Constantinescu, J.-W. Jeong, X. Li, D. K. Scott, K.-I. Jang, H.-J. Chung, J. A. Rogers, J. Rieger, Epidermal electronics for electromyography: An application to swallowing therapy. *Med. Eng. Phys.* **38**, 807–812 (2016).
7. K. K. Kim, M. Kim, K. Pyun, J. Kim, J. Min, S. Koh, S. E. Root, J. Kim, B.-N. T. Nguyen, Y. Nishio, S. Han, J. Choi, C.-Y. Kim, J. B.-H. Tok, S. Jo, S. H. Ko, Z. Bao, A substrate-less nanomesh receptor with meta-learning for rapid hand task recognition. *Nat. Electron.* **6**, 64–75 (2022).
8. J.-W. Jeong, W.-H. Yeo, A. Akhtar, J. J. S. Norton, Y.-J. Kwack, S. Li, S.-Y. Jung, Y. Su, W. Lee, J. Xia, H. Cheng, Y. Huang, W.-S. Choi, T. Bretl, J. A. Rogers, Materials and optimized designs for human-machine interfaces via epidermal electronics. *Adv. Mater.* **25**, 6839–6846 (2013).
9. L. Tian, B. Zimmerman, A. Akhtar, K. J. Yu, M. Moore, J. Wu, R. J. Larsen, J. W. Lee, J. Li, Y. Liu, B. Metzger, S. Qu, X. Guo, K. E. Mathewson, J. A. Fan, J. Cornman, M. Fatina, Z. Xie, Y. Ma, J. Zhang, Y. Zhang, F. Dolcos, M. Fabiani, G. Gratton, T. Bretl, L. J. Hargrove, P. V. Braun, Y. Huang, J. A. Rogers, Large-area MRI-compatible epidermal electronic interfaces for prosthetic control and cognitive monitoring. *Nat. Biomed. Eng.* **3**, 194–205 (2019).
10. F. Stauffer, M. Thielen, C. Sauter, S. Chardonnens, S. Bachmann, K. Tybrandt, C. Peters, C. Hierold, J. Vörös, Skin conformal polymer electrodes for clinical ECG and EEG recordings. *Adv. Healthc. Mater.* **7**, e1700994 (2018).
11. J. Li, Y. Ma, D. Huang, Z. Wang, Z. Zhang, Y. Ren, M. Hong, Y. Chen, T. Li, X. Shi, L. Cao, J. Zhang, B. Jiao, J. Liu, H. Sun, Z. Li, High-performance flexible microneedle array as a low-impedance surface biopotential dry electrode for wearable electrophysiological recording and polysomnography. *Nanomicro Lett.* **14**, 132 (2022).
12. H. Lim, H. S. Kim, R. Qazi, Y. Kwon, J. Jeong, W. Yeo, Advanced soft materials, sensor integrations, and applications of wearable flexible hybrid electronics in healthcare, energy, and environment. *Adv. Mater.* **32**, e1901924 (2020).
13. Y. Luo, M. R. Abidian, J.-H. Ahn, D. Akinwande, A. M. Andrews, M. Antonietti, Z. Bao, M. Berggren, C. A. Berkey, C. J. Bettinger, J. Chen, P. Chen, W. Cheng, X. Cheng, S.-J. Choi, A. Chortos, C. Dagdeviren, R. H. Dauskardt, C. Di, M. D. Dickey, X. Duan, A. Facchetti, Z. Fan, Y. Fang, J. Feng, X. Feng, H. Gao, W. Gao, X. Gong, C. F. Guo, X. Guo, M. C. Hartel, Z. He, J. S. Ho, Y. Hu, Q. Huang, Y. Huang, F. Huo, M. M. Hussain, A. Javey, U. Jeong, C. Jiang, X. Jiang, J. Kang, D. Karnaushenko, A. Khademhosseini, D.-H. Kim, I.-D. Kim, D. Kireev, L. Kong, C. Lee, N.-E. Lee, P. S. Lee, T.-W. Lee, F. Li, J. Li, C. Liang, C. T. Lim, Y. Lin, D. J. Lipomi, J. Liu, K. Liu, N. Liu, R. Liu, Y. Liu, Y. Liu, Z. Liu, Z. Liu, X. J. Loh, N. Lu, Z. Lv, S. Magdassi, G. G. Malliaras, N. Matsuhisa, A. Nathan, S. Niu, J. Pan, C. Pang, Q. Pei, H. Peng, D. Qi, H. Ren, J. A. Rogers, A. Rowe, O. G. Schmidt, T. Sekitani, D.-G. Seo, G. Shen, X. Sheng, Q. Shi, T. Someya, Y. Song, E. Stavrinidou, M. Su, X. Sun, K. Takei, X.-M. Tao, B. C. K. Tee, A. V.-Y. Thean, T. Q. Trung, C. Wan, H. Wang, J. Wang, M. Wang, S. Wang, T. Wang, Z. L. Wang, P. S. Weiss, H. Wen, S. Xu, T. Xu, H. Yan, X. Yan, H. Yang, L. Yang, S. Yang, L. Yin, C. Yu, G. Yu, J. Yu, S.-H. Yu, X. Yu, E. Zamburg, H. Zhang, X. Zhang, X. Zhang, X. Zhang, Y. Zhang, Y. Zhang, S. Zhao, X. Zhao, Y. Zheng, Y.-Q. Zheng, Z. Zheng, T. Zhou, B. Zhu, M. Zhu, R. Zhu, Y. Zhu, Y. Zhu, G. Zou, X. Chen, Technology roadmap for flexible sensors. *ACS Nano* **17**, 5211–5295 (2023).
14. M. Baumgartner, F. Hartmann, M. Drack, D. Preninger, D. Wirthl, R. Gerstmayr, L. Lehner, G. Mao, R. Pruckner, S. Demchyshyn, L. Reiter, M. Strobel, T. Stockinger, D. Schiller, S. Kimeswenger, F. Greibich, G. Buchberger, E. Bradt, S. Hild, S. Bauer, M. Kaltenbrunner, Resilient yet entirely degradable gelatin-based biogels for soft robots and electronics. *Nat. Mater.* **19**, 1102–1109 (2020).
15. P. A. Lopes, D. Vaz Gomes, D. Green Marques, P. Faia, J. Góis, T. F. Patrício, J. Coelho, A. Serra, A. T. de Almeida, C. Majidi, M. Tavakoli, Soft bioelectronic stickers: Selection and evaluation of skin-interfacing electrodes. *Adv. Healthc. Mater.* **8**, e1900234 (2019).
16. T. C. Ferree, P. Luu, G. S. Russell, D. M. Tucker, Scalp electrode impedance, infection risk, and EEG data quality. *Clin. Neurophysiol.* **112**, 536–544 (2001).
17. R. A. Nawrocki, H. Jin, S. Lee, T. Yokota, M. Sekino, T. Someya, Self-adhesive and ultra-conformable, sub-300 nm dry thin-film electrodes for surface monitoring of biopotentials. *Adv. Funct. Mater.* **28**, 1803279 (2018).
18. R. M. Green, W. J. Messick, J. J. Ricotta, M. H. Charlton, R. Satran, M. M. McBride, J. A. DeWeese, Benefits, shortcomings, and costs of EEG monitoring. *Ann. Surg.* **201**, 785–792 (1985).
19. R. J. Cochran, T. Rosen, Contact dermatitis caused by ECG electrode paste. *South. Med. J.* **73**, 1667–1668 (1980).
20. R. J. Coskey, Contact dermatitis caused by ECG electrode jelly. *Arch. Dermatol.* **113**, 839–840 (1977).
21. W. Uter, H. J. Schwanitz, Contact dermatitis from propylene glycol in ECG electrode gel. *Contact Dermatitis* **34**, 230–231 (1996).
22. Y. Zhao, S. Zhang, T. Yu, Y. Zhang, G. Ye, H. Cui, C. He, W. Jiang, Y. Zhai, C. Lu, X. Gu, N. Liu, Ultra-conformal skin electrodes with synergistically enhanced conductivity for long-time and low-motion artifact epidermal electrophysiology. *Nat. Commun.* **12**, 4880 (2021).
23. F. Ershad, A. Thukral, J. Yue, P. Comeaux, Y. Lu, H. Shim, K. Sim, N.-I. Kim, Z. Rao, R. Guevara, L. Contreras, F. Pan, Y. Zhang, Y.-S. Guan, P. Yang, X. Wang, P. Wang, X. Wu, C. Yu,

Ultra-conformal drawn-on-skin electronics for multifunctional motion artifact-free sensing and point-of-care treatment. *Nat. Commun.* **11**, 3823 (2020).
24. D.-H. Kim, N. Lu, R. Ma, Y.-S. Kim, R.-H. Kim, S. Wang, J. Wu, S. M. Won, H. Tao, A. Islam, K. J. Yu, T. Kim, R. Chowdhury, M. Ying, L. Xu, M. Li, H.-J. Chung, H. Keum, M. McCormick, P. Liu, Y.-W. Zhang, F. G. Omenetto, Y. Huang, T. Coleman, J. A. Rogers, Epidermal electronics. *Science* **333**, 838–843 (2011).
25. J. J. S. Norton, D. S. Lee, J. W. Lee, W. Lee, O. Kwon, P. Won, S.-Y. Jung, H. Cheng, J.-W. Jeong, A. Akce, S. Umunna, I. Na, Y. H. Kwon, X.-Q. Wang, Z. Liu, U. Paik, Y. Huang, T. Bretl, W.-H. Yeo, J. A. Rogers, Soft, curved electrode systems capable of integration on the auricle as a persistent brain–computer interface. *Proc. Natl. Acad. Sci. U.S.A.* **112**, 3920–3925 (2015).
26. K.-I. Jang, H. N. Jung, J. W. Lee, S. Xu, Y. H. Liu, Y. Ma, J.-W. Jeong, Y. M. Song, J. Kim, B. H. Kim, A. Banks, J. W. Kwak, Y. Yang, D. Shi, Z. Wei, X. Feng, U. Paik, Y. Huang, R. Ghaffari, J. A. Rogers, Ferromagnetic, folded electrode composite as a soft interface to the skin for long-term electrophysiological recording. *Adv. Funct. Mater.* **26**, 7281–7290 (2016).
27. M. Mahmood, S. Kwon, H. Kim, Y. Kim, P. Siriaraya, J. Choi, B. Otkhmezuri, K. Kang, K. J. Yu, Y. C. Jang, C. S. Ang, W. Yeo, Wireless soft scalp electronics and virtual reality system for motor imagery-based brain–machine interfaces. *Adv. Sci.* **8**, e2101129 (2021).
28. Y. Fu, J. Zhao, Y. Dong, X. Wang, Dry electrodes for human bioelectrical signal monitoring. *Sensors* **20**, 3651 (2020).
29. Z. Yan, D. Xu, Z. Lin, P. Wang, B. Cao, H. Ren, F. Song, C. Wan, L. Wang, J. Zhou, X. Zhao, J. Chen, Y. Huang, X. Duan, Highly stretchable van der Waals thin films for adaptable and breathable electronic membranes. *Science* **375**, 852–859 (2022).
30. G. Lee, H. Woo, C. Yoon, C. Yang, J. Bae, W. Kim, D. H. Lee, H. Kang, S. Han, S. Kang, S. Park, H. Kim, J. Jeong, S. Park, A personalized electronic tattoo for healthcare realized by on-the-spot assembly of an intrinsically conductive and durable liquid-metal composite. *Adv. Mater.* **34**, e2204159 (2022).
31. L. Ren, B. Liu, W. Zhou, L. Jiang, A mini review of microneedle array electrode for bio-signal recording: A review. *IEEE Sens. J.* **20**, 577–590 (2020).
32. L. Ren, Q. Jiang, Z. Chen, K. Chen, S. Xu, J. Gao, L. Jiang, Flexible microneedle array electrode using magnetorheological drawing lithography for bio-signal monitoring. *Sens. Actuators A: Phys.* **268**, 38–45 (2017).
33. R. Wang, X. Jiang, W. Wang, Z. Li, A microneedle electrode array on flexible substrate for long-term EEG monitoring. *Sens. Actuators B* **244**, 750–758 (2017).
34. H. Zhang, W. Pei, Y. Chen, X. Guo, X. Wu, X. Yang, H. Chen, A motion interference-insensitive flexible dry electrode. *IEEE Trans. Biomed. Eng.* **63**, 1136–1144 (2016).
35. L. Ren, S. Xu, J. Gao, Z. Lin, Z. Chen, B. Liu, L. Liang, L. Jiang, Fabrication of flexible microneedle array electrodes for wearable bio-signal recording. *Sensors* **18**, 1191 (2018).
36. M. Rajabi, N. Roxhed, R. Z. Shafagh, T. Haraldson, A. C. Fischer, Flexible and stretchable microneedle patches with integrated rigid stainless steel microneedles for transdermal biointerfacing. *PLOS One* **11**, e0166330 (2016).
37. S. Wang, H. Zhou, G. Dang, C. Chen, Synthesis and characterization of thermally stable, high-modulus polyimides containing benzimidazole moieties. *J. Polym. Sci. A Polym. Chem.* **47**, 2024–2031 (2009).
38. K. Miyake, N. Satomi, S. Sasaki, Elastic modulus of polystyrene film from near surface to bulk measured by nanoindentation using atomic force microscopy. *Appl. Phys. Lett.* **89**, 031925 (2006).
39. R. P. von Metzen, T. Stieglitz, The effects of annealing on mechanical, chemical, and physical properties and structural stability of Parylene C. *Biomed. Microdevices* **15**, 727–735 (2013).
40. C. F. Guimarães, L. Gasperini, A. P. Marques, R. L. Reis, The stiffness of living tissues and its implications for tissue engineering. *Nat. Rev. Mater.* **5**, 351–370 (2020).
41. Z. Wang, A. A. Volinsky, N. D. Gallant, Crosslinking effect on polydimethylsiloxane elastic modulus measured by custom-built compression instrument. *J. Appl. Polym. Sci.* **131**, 41050 (2014).
42. G. S. Guvanasen, L. Guo, R. J. Aguilar, A. L. Cheek, C. S. Shafor, S. Rajaraman, T. R. Nichols, S. P. DeWeerth, A stretchable microneedle electrode array for stimulating and measuring intramuscular electromyographic activity. *IEEE Trans. Neural Syst. Rehabil. Eng.* **25**, 1440–1452 (2017).
43. D. Byun, S. J. Cho, S. Kim, Fabrication of a flexible penetrating microelectrode array for use on curved surfaces of neural tissues. *J. Micromech. Microeng.* **23**, 125010 (2013).
44. M. A. Hopcroft, W. D. Nix, T. W. Kenny, What is the Young's modulus of silicon? *J. Microelectromech. Syst.* **19**, 229–238 (2010).
45. P. G. Agache, C. Monneur, J. L. Leveque, J. De Rigal, Mechanical properties and Young's modulus of human skin in vivo. *Arch. Dermatol. Res.* **269**, 221–232 (1980).
46. C. Czekalla, K. H. Schönborn, J. Lademann, M. C. Meinke, Noninvasive determination of epidermal and stratum corneum thickness in vivo using two-photon microscopy and optical coherence tomography: Impact of body area, age, and gender. *Skin Pharmacol. Physiol.* **32**, 142–150 (2019).
47. J. M. Benítez, F. J. Montáns, The mechanical behavior of skin: Structures and models for the finite element analysis. *Comput. Struct.* **190**, 75–107 (2017).
48. K. van der Maaden, W. Jiskoot, J. Bouwstra, Microneedle technologies for (trans)dermal drug and vaccine delivery. *J. Control. Release* **161**, 645–655 (2012).
49. R. Maiti, L.-C. Gerhardt, Z. S. Lee, R. A. Byers, D. Woods, J. A. Sanz-Herrera, S. E. Franklin, R. Lewis, S. J. Matcher, M. J. Carré, In vivo measurement of skin surface strain and sub-surface layer deformation induced by natural tissue stretching. *J. Mech. Behav. Biomed. Mater.* **62**, 556–569 (2016).
50. J. R. Greer, W. C. Oliver, W. D. Nix, Size dependence of mechanical properties of gold at the micron scale in the absence of strain gradients. *Acta Mater.* **53**, 1821–1830 (2005).
51. F. Avile´s, L. Llanes, A. I. Oliva, J. E. Corona, M. Aguilar-Vega, M. I. Lori´a-Bastarrachea, in *Elasto-Plastic Properties of Thin Gold Films Over Polymeric Substrates* (American Society of Mechanical Engineers Digital Collection, 2009), pp. 593–594.
52. N. Lu, C. Lu, S. Yang, J. Rogers, Highly sensitive skin-mountable strain gauges based entirely on elastomers. *Adv. Funct. Mater.* **22**, 4044–4050 (2012).
53. C. Y. Kim, M. J. Ku, R. Qazi, H. J. Nam, J. W. Park, K. S. Nam, S. Oh, I. Kang, J.-H. Jang, W. Y. Kim, J.-H. Kim, J.-W. Jeong, Soft subdermal implant capable of wireless battery charging and programmable controls for applications in optogenetics. *Nat. Commun.* **12**, 535 (2021).
54. W. Guo, P. Zheng, X. Huang, H. Zhuo, Y. Wu, Z. Yin, Z. Li, H. Wu, Matrix-independent highly conductive composites for electrodes and interconnects in stretchable electronics. *ACS Appl. Mater. Interfaces* **11**, 8567–8575 (2019).
55. K. Zhu, W. Guo, G. Yang, Z. Li, H. Wu, High-fidelity recording of EMG signals by multichannel on-skin electrode arrays from target muscles for effective human–machine interfaces. *ACS Appl. Electron. Mater.* **3**, 1350–1358 (2021).
56. Z. Li, T. Le, Z. Wu, Y. Yao, L. Li, M. Tentzeris, K.-S. Moon, C. P. Wong, Rational design of a printable, highly conductive silicone-based electrically conductive adhesive for stretchable radio-frequency antennas. *Adv. Funct. Mater.* **25**, 464–470 (2015).
57. R. Xie, Q. Li, L. Teng, Z. Cao, F. Han, Q. Tian, J. Sun, Y. Zhao, M. Yu, D. Qi, P. Guo, G. Li, F. Huo, Z. Liu, Strenuous exercise-tolerance stretchable dry electrodes for continuous multi-channel electrophysiological monitoring. *NPJ Flex. Electron.* **6**, 75 (2022).
58. A. Miyamoto, S. Lee, N. F. Cooray, S. Lee, M. Mori, N. Matsuhisa, H. Jin, L. Yoda, T. Yokota, A. Itoh, M. Sekino, H. Kawasaki, T. Ebihara, M. Amagai, T. Someya, Inflammation-free, gas-permeable, lightweight, stretchable on-skin electronics with nanomeshes. *Nat. Nanotechnol.* **12**, 907–913 (2017).
59. Y. Hou, Z. Li, Z. Wang, H. Yu, Miura-ori structured flexible microneedle array electrode for biosignal recording. *Microsyst. Nanoeng.* **7**, 53 (2021).
60. K.-I. Jang, S. Y. Han, S. Xu, K. E. Mathewson, Y. Zhang, J.-W. Jeong, G.-T. Kim, R. C. Webb, J. W. Lee, T. J. Dawidczyk, R. H. Kim, Y. M. Song, W.-H. Yeo, S. Kim, H. Cheng, S. I. Rhee, J. Chung, B. Kim, H. U. Chung, D. Lee, Y. Yang, M. Cho, J. G. Gaspar, R. Carbonari, M. Fabiani, G. Gratton, Y. Huang, J. A. Rogers, Rugged and breathable forms of stretchable electronics with adherent composite substrates for transcutaneous monitoring. *Nat. Commun.* **5**, 4779 (2014).
61. American Society for Testing and Materials, ASTM E96: Standard Test Methods for Water Vapor Transmission of Materials (1995); http://archive.org/details/gov.law.astm.e96.1995.
62. A. C. Karwoski, R. H. Plaut, Experiments on peeling adhesive tapes from human forearms. *Skin Res. Technol.* **10**, 271–277 (2004).
63. G. Li, S. Wang, Y. Y. Duan, Towards conductive-gel-free electrodes: Understanding the wet electrode, semi-dry electrode and dry electrode-skin interface impedance using electrochemical impedance spectroscopy fitting. *Sens. Actuators B* **277**, 250–260 (2018).
64. E. Lamers, T. H. S. van Kempen, F. P. T. Baaijens, G. W. M. Peters, C. W. J. Oomens, Large amplitude oscillatory shear properties of human skin. *J. Mech. Behav. Biomed. Mater.* **28**, 462–470 (2013).
65. S.-H. Byun, J. Y. Sim, Z. Zhou, J. Lee, R. Qazi, M. C. Walicki, K. E. Parker, M. P. Haney, S. H. Choi, A. Shon, G. B. Gereau, J. Bilbily, S. Li, Y. Liu, W.-H. Yeo, J. G. McCall, J. Xiao, J.-W. Jeong, Mechanically transformative electronics, sensors, and implantable devices. *Sci. Adv.* **5**, eaay0418 (2019).
66. P. R. Cavanagh, P. V. Komi, Electromechanical delay in human skeletal muscle under concentric and eccentric contractions. *Eur. J. Appl. Physiol. Occup. Physiol.* **42**, 159–163 (1979).
67. A. J. Young, D. P. Ferris, State of the art and future directions for lower limb robotic exoskeletons. *IEEE Trans. Neural Syst. Rehabil. Eng.* **25**, 171–182 (2017).
68. J. Kim, P. Kantharaju, H. Yi, M. Jacobson, H. Jeong, H. Kim, J. Lee, J. Matthews, N. Zavanelli, H. Kim, H. Jeong, M. Kim, W.-H. Yeo, Soft wearable flexible bioelectronics integrated with an ankle-foot exoskeleton for estimation of metabolic costs and physical effort. *NPJ Flex. Electron.* **7**, 3 (2023).
69. U. Heo, J. Feng, S. J. Kim, J. Kim, sEMG-triggered fast assistance strategy for a pneumatic back support exoskeleton. *IEEE Trans. Neural Syst. Rehabil. Eng.* **30**, 2175–2185 (2022).
70. U. Heo, S. J. Kim, J. Kim, Backdrivable and fully-portable pneumatic back support exoskeleton for lifting. *IEEE Robot. Autom. Lett.* **5**, 2047–2053 (2020).

Acknowledgments
Funding: This work was supported by the National Research Foundation of Korea (NRF-2020M3C1B8A01111568 and NRF-2022M3E5E9017759) and BK21 FOUR (Connected AI Education & Research Program for Industry and Society Innovation, KAIST EE, No. 4120200113769). **Author contributions:** Concept, design, and study direction: H.K., J.L., and J.-W.J. Device fabrication: H.K., Y.O., and B.C. Experimental validation: H.K., J.L., U.H., Y.K., H.J., S.P., J.K., and J.-W.J. Data analysis: H.K., J.L., Y.K., Y.O., B.C., and J.-W.J. Theoretical modeling: H.K., D.K.J., and J.X. Manuscript writing: H.K., J.L., K.-C.A., C.Y.K., S.-H.B., and J.-W.J. Supervision: W.-H.Y., Z.L., S.P., J.X., J.K., and J.-W.J. Projection administration: J.-W.J. **Competing interests:** The authors declare that they have no competing interests. **Data and materials availability:** All data needed to evaluate the conclusions in the paper are present in the paper and/or the Supplementary Materials.

Submitted 28 August 2023
Accepted 18 December 2023
Published 17 January 2024
10.1126/sciadv.adk5260

ScienceAdvances

Skin preparation–free, stretchable microneedle adhesive patches for reliable electrophysiological sensing and exoskeleton robot control

Heesoo Kim, Juhyun Lee, Ung Heo, Dhileep Kumar Jayashankar, Karen-Christian Agno, Yeji Kim, Choong Yeon Kim, Youngjun Oh, Sang-Hyuk Byun, Bohyung Choi, Hwayeong Jeong, Woon-Hong Yeo, Zhuo Li, Seongjun Park, Jianliang Xiao, Jung Kim, and Jae-Woong Jeong

Sci. Adv. **10** (3), eadk5260. DOI: 10.1126/sciadv.adk5260

Science Advances (ISSN 2375-2548) is published by the American Association for the Advancement of Science. 1200 New York Avenue NW, Washington, DC 20005. The title *Science Advances* is a registered trademark of AAAS.